Optical readout of MicroPattern Gaseous Detectors with SiPMs

CERN Summer Student Program 2022

Jesse Woods

Supervised by Florian Brunbauer and Eraldo Oliveri

EP-DT-DD GDD
CERN
Switzerland

August 2022

1 Introduction

1.1 Motivation

In order to probe the universe for new and exciting physics, increasingly higher and higher energy scales must be accessed to test our theories, potentially uncovering new particles and interactions. Particle colliders are one such technology that allow us to do this.

With the ever increasing luminosity of new particle colliders, such as the High-Luminosity LHC planned to begin operation in 2029, there is demand for detectors capable of taking advantage of this luminosity. The luminosity measures the number of collision events occurring in a given time-frame, and thus it is crucial that detectors operate with a finer and finer temporal resolution to keep up with these advances. This timing data is not only useful for discerning between events, but also for particle track reconstruction, by using spatial data over multiple layers of detectors.

Thus, detector development is an active area of research, as these detectors must not only be fast, but also reliable and scalable. A particular type of detector that is of interest is the Gas Electron Multiplier (GEM). Such GEMs already exist in the CMS experiment at the LHC, for muon detection. These sorts of detectors are part of a larger class of detectors known as Micropattern gaseous detectors (MPGDs), named from the fact the each detector contains a micro structure (for example a mesh, or a plate with small holes on the tens of micros scale), that along with the gas inside, allow for very efficient amplification of electronic signals. This has the advantage of making the signals less prone to noise. These detectors also have the advantage of being tolerant to radiation, something of high importance in the particle collider setting.

The Gas Detector Development (GDD) lab at CERN designs and tests new prototypes for MPGDs, with the goal of achieving timing resolution on the picosecond scale, while being both robust and scalable. In particular, this project focused on marrying the Micro-Mesh Gaseous Structure (MicroMegas) detector with optical Silicon Photomulitpliers (SiPMs), to investigate whether the fast timing of the Micromegas can be corroborated with the superior spatial resolution of the SiPMs, to allow for better overall resolution for detecting muons and electrons.

1.2 Theory

The basic function of a MPGD is to convert incoming radiation to electrons, which are then amplified to create a strong electronic signal at readout.

This signal can be generated through a variety of pathways.

Firstly, when used to detect charged particles, the Cherenkov radiation mechanism can be used. When particles move through matter faster than the speed of light in that material (for instance, when the relativistic speed particles of a particle collider enter a crystal), a "Cherenkov cone" of light is produced around the particle. Detectors can be designed to include a Cherenkov crystal, such as MgF_2, and the light produced is of a short enough wavelength to induce the photoelectric effect in a photocathode. This allows for effectively the conversion of particles to electrons, which then enter the body of the detector.

Inside a Micromega detector, there are two regions. When the electron enters the detector, it leaves the cathode and is in the drift region. This region has a weak electric field, and as the name suggests, is primarily to "drift" these primary electrons away from the photocathode, towards the grounded mesh component. These electrons then enter an amplification region. In the GEM devices, due to the boundary conditions of the mesh layer, the holes have a high electric flux density. For the Micromega devices, the region between the mesh and the anode has a high electric flux density. Thus, electrons passing through this region experience an extreme amount of acceleration. These electrons now have the capability to ionise the gas molecules inside the detector, which in turn ionise more gas molecules, creating an avalanche amplification effect. Particular gas mixtures are chosen that have high electron gain through this pathway and have been optimised by the COMPASS collaboration, such as Ne:C_2H_4:CF_4, 80:10:10.

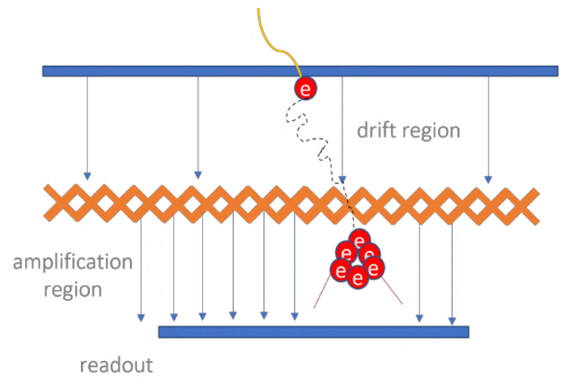

Figure 1: Diagram of a Micromega detector, with Cherenkov crystal and photocathode in the top layer, mesh in the centre, and anode at the bottom. The yellow line represents incident radiation.

During this avalanche process, additional light may be produced if the gas is left in an excited state. This is known as scintillation. The gas mixture can be designed in order to maximise scintillation. If this scintillation light is in the visible region (or UV, with suitable devices) optical readout can be performed.

In this project, we will use Silicon Photomultipliers to perform optical readout on this scintillation light. We will then measure the timing parameters of such a signal, and aim to determine the optimal way of operating such devices in this scenario.

2 Experiment

In this project, Micromegas were tested as part of the July 2022 test beam campaign, to detect muons created by using CERN's SPS proton beam fired at a target. In order to discern the best resolutions of the detector, five different Hamamatsu SiPMs were to be tested. Each SiPM has a different size and capacitance. The aim was to find the optimal SiPM size. While a larger SiPM is able to detect more light due to its large area, producing a better signal, it will also have a larger capacitance which decreases the temporal resolution.

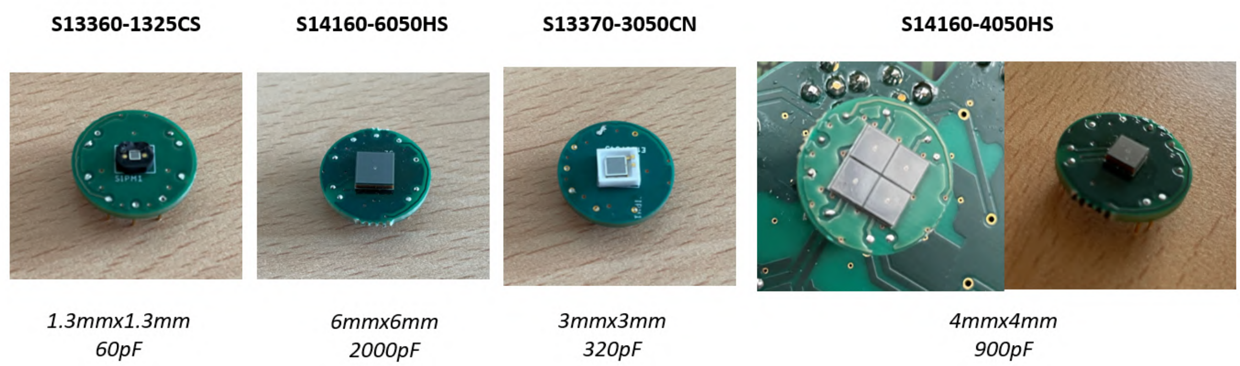

Figure 2: The five SiPM devices that were tested, with specifications.

Note that one of the SiPMs, the S13370-3050CS, is UV sensitive, potentially allowing for the collection of more light and thus a better signal. In order to take advantage of this UV sensitivity, an 80:20 Ar:CF_4 gas mixture was used. This particular gas produces a good amount of scintillation light in the visible spectrum, as well as in the UV.

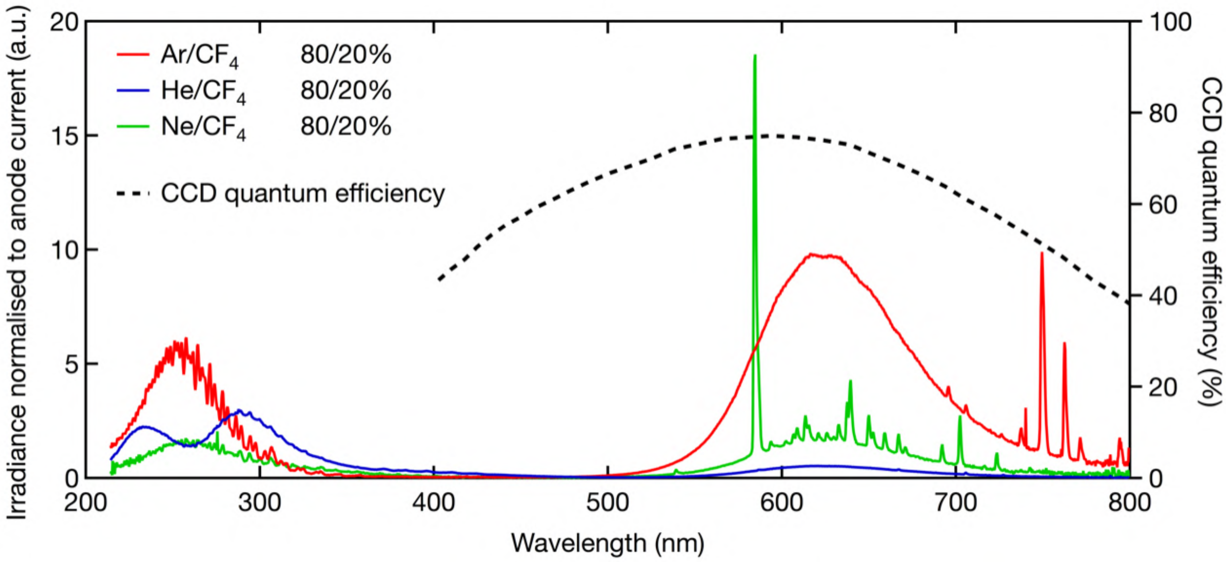

Figure 3: Scintillation spectrum of various gases, including Ar:CF_4. Note the higher proportion of light produced by Ar:CF_4 than the other gases. [1]

In order to detect this light, the anode mustn't be opaque. There were two anodes under test for this experiment: Cr, and ITO. Cr has the advantage of being highly transmissive of both visible and UV light, making a good candidate for the anode. However, due to the very small thickness (nms) of the Cr layer, it is also highly sensitive to light and moisture, and can easily be damaged. Particularly, it is sensitive to sparks that occur in the device which can evaporate away the Cr. This material caused difficulty during the experiment due to its sensitive nature, and thus in the end we opted for ITO. This was unfortunate, as ITO is essentially opaque to UV radiation, meaning that we could not take advantage of the UV sensitivity of the S13370-3050CS device.

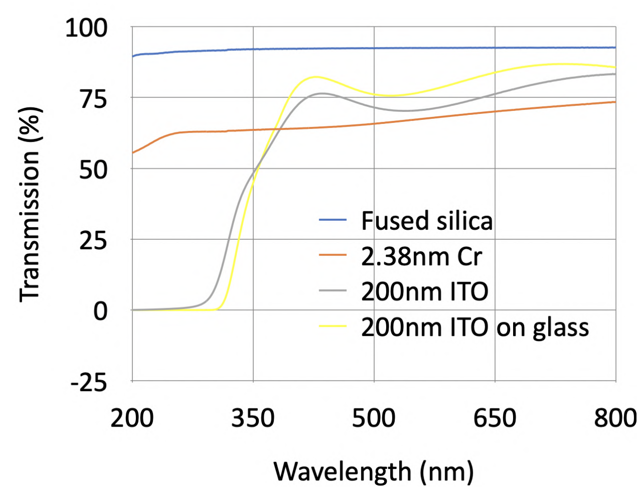

Figure 4: Transmission rate of anode materials. [1]

Prior to the experiment, the Micromega was mounted inside a gas chamber in the clean room, which was then flushed 3 times with Ar to remove all unwanted gases and moisture. It was then filled to slight overpressure with the Ar:CF_4 mixture in order to be able to check the integrity of the chamber throughout the experiment by measuring the pressure. Having the chamber in overpressure rather than underpressure meant that any leakages would result in the escape of gas, maintaining the gas quality inside. The SiPMs were mounted on a separate

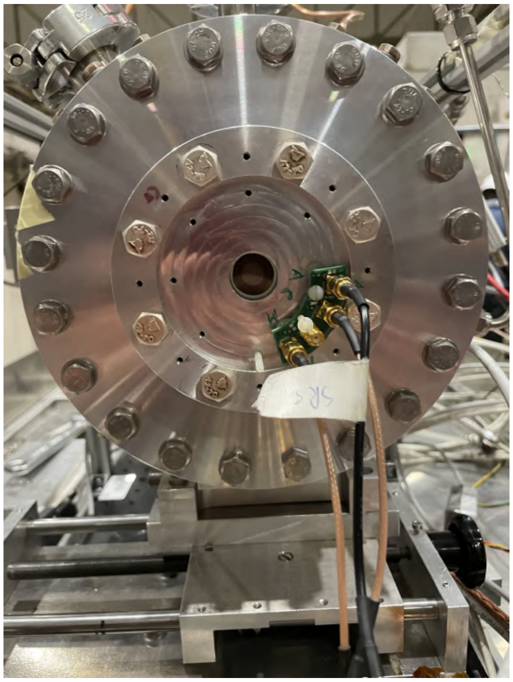

Figure 5: Gas chamber (beam direction out of page). Note the small window where the SiPM will be mounted.

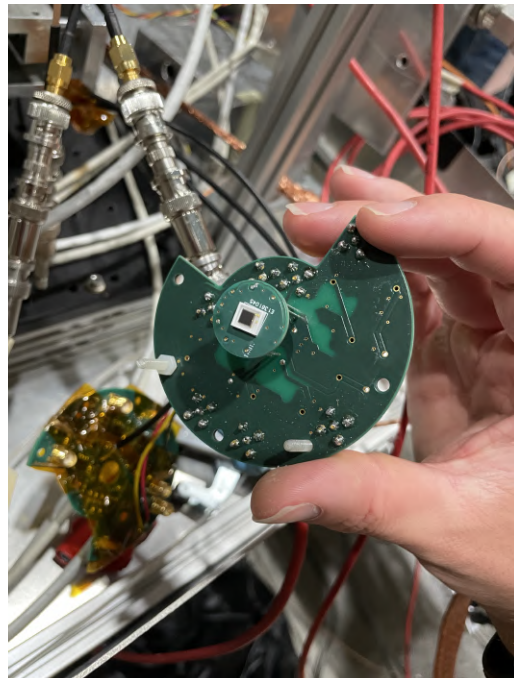

Figure 6: SiPM on PCB. The small SiPM PCB is attached to the main PCB via long pins, and can be removed and exchanged for a different device.

PCB, which could be mounted and dismounted from the chamber without opening it, that faced a small window on the gas chamber in order to be able to detect the scintillation light.

The chamber was then brought to the test beam area for experiment. The chamber was placed in the beam, downstream from an already calibrated MCP to be used for a timing reference, and upstream from three GEMs which were used for spatial reconstruction to determine through which part of the detector a detected particle was incident and check to see if this correlates with the detector readout. This was to be done in software. When in use, the chamber was covered by two opaque blankets. This was done to stop any external light from being detected by the SiPMs, leaving only the scintillation light to be detected from inside the chamber. The chamber and other circuit components were also grounded to reduce signal noise

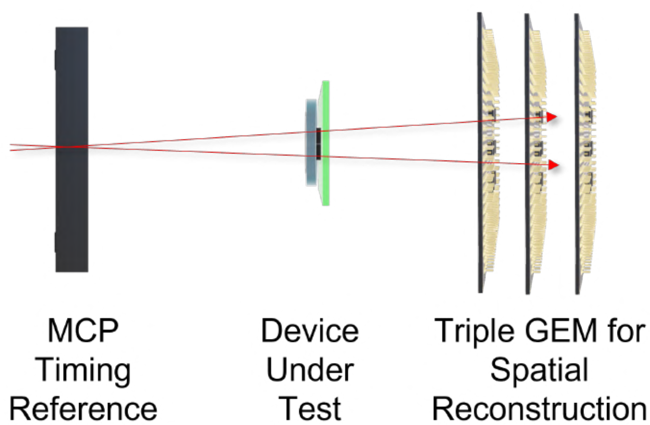

Figure 7: Experimental setup.

To begin the experiment, the chamber was firstly aligned by using the triple GEM setup to determine the position of the chamber relative to the beam. The chamber position was then incrementally adjusted by physically moving it, in order to be centered on the beam and thus provide the best quality data. This is important, as a centered beam allows for the maximum collection of light from the Cherenkov cone. Several calibration runs were performed in order to ensure the chamber was positioned correctly. Data was obtained by measuring the detector output with an oscilloscope, which was controlled remotely. Before obtaining any measurements, the cathode and anode voltages, as well as the SiPM voltage, were adjusted in order to have as high gain as possible without causing sparks inside the detector, which could damage it. The voltages were also set low enough to reduce dark count events, only detecting particles of sufficient energy. Measurements were then performed for a few different voltages inside this acceptable range, for each of the devices. The oscilloscope was set to trigger off the MCP signal, thus allowing for us to distinguish between events in our detector by correlating them with the MCP trigger. The oscilloscope voltage scale was also adjusted so that in general the signal was near the window maximum amplitude to allow for the finest resolution in our recorded signal. Note that some events (sparks, unusually high energy particles) would max out the oscilloscope amplitude, however, a maximum threshold was chosen such that these were somewhat infrequent, and any such spikes were excluded from the analysis.

3 Results

Several sets of data were collected for SiPM device, ranging over a small set of anode/cathode and device voltages. These were then imported into matlab to process. Some example waveforms that were extracted from this data can be seen in Figure 8 and Figure 9

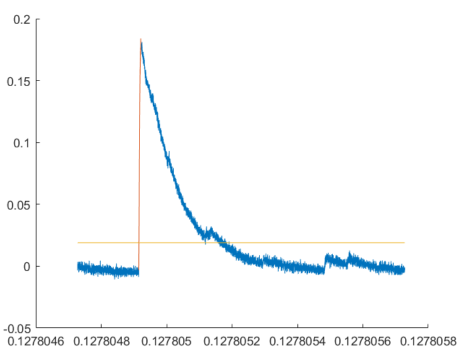

Figure 8: Example waveform extracted from data. The time axis is time after MCP tigger.

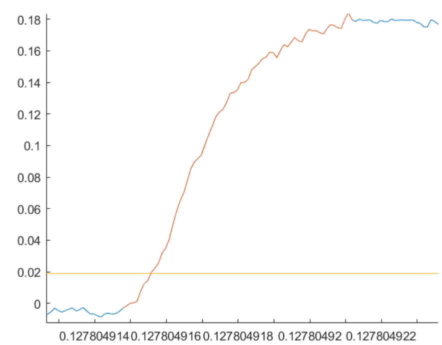

Figure 9: Zoomed waveform in order to see detail in the signal's rising edge.

In the preliminary analysis, some statistics about the signals were measured. Firstly, a distribution of risetimes of the signals were constructed for each device to gain a rough idea of the characterstics of the device. Note that a voltage threshold was used on the amplitude of these signals to filter out noise. This threshold was selected by viewing a sample subset of the waveforms for each device and tuning the threshold to reject null events. Each of these can be seen in Figures 10 to 24.

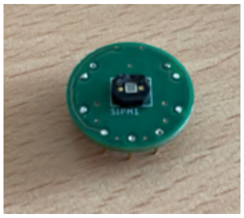

Figure 10: S13360-1325CS device.

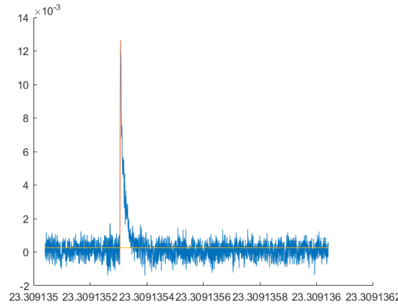

Figure 11: Sample S13360-1325CS waveform.

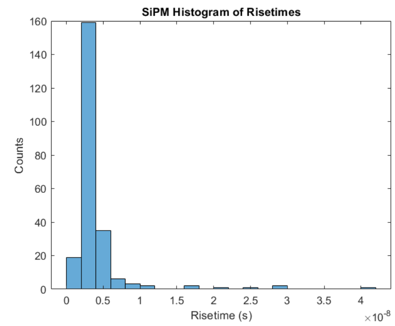

Figure 12: Distribution of S13360-1325CS risetimes.

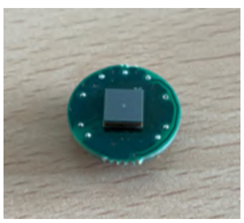

Figure 13: S14160-6050HS device.

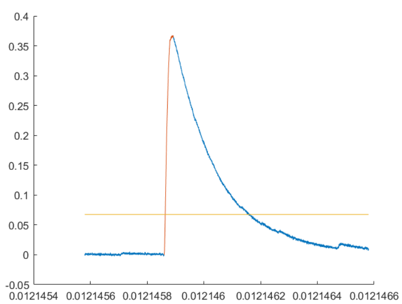

Figure 14: Sample S14160-6050HS waveform.

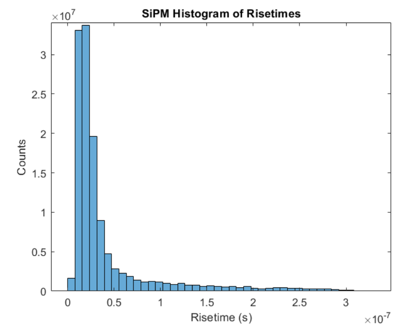

Figure 15: Distribution of S14160-6050HS risetimes.

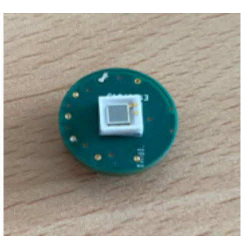

Figure 16: VUV S13370-3050CS device.

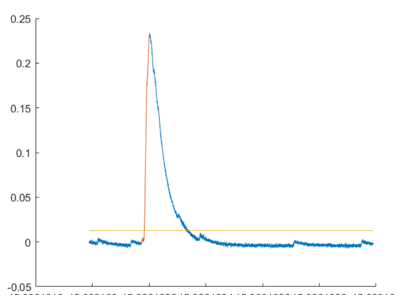

Figure 17: Sample S13370-3050CS waveform.

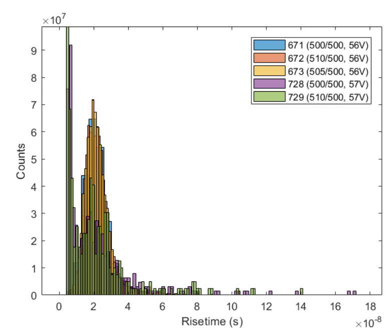

Figure 18: Distribution of S13370-3050CS risetimes.

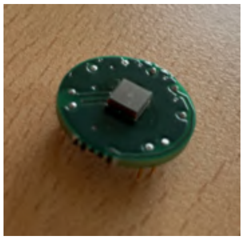

Figure 19: Single S14160-4050HS device.

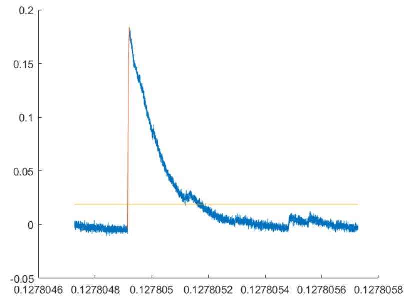

Figure 20: Sample S14160-4050HS waveform.

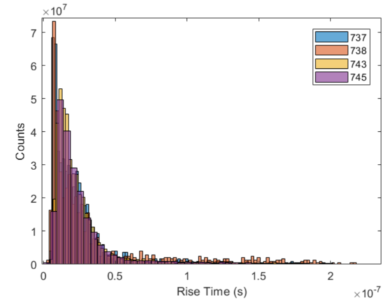

Figure 21: Distribution of S14160-4050HS risetimes.

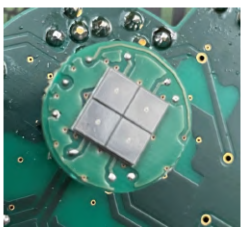

Figure 22: 4 Panel S14160-4050HS device.0

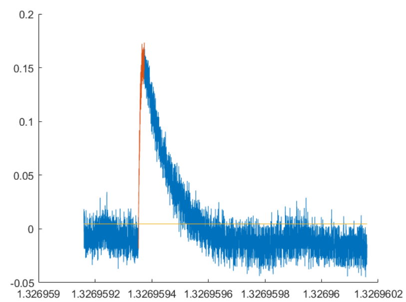

Figure 23: Sample S14160-4050HS waveform.

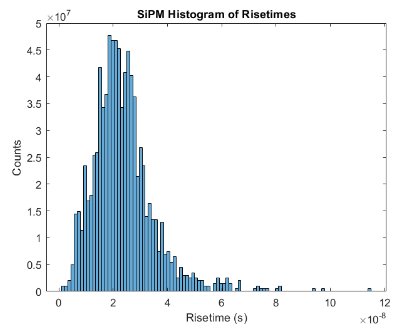

Figure 24: Distribution of S14160-4050HS risetimes.

Note that some of these signals were anomalous, for example having unreasonable short risetimes or saturated amplitudes. A likely culprit would be a spark in the device at the same time as a signal triggered by the MCP. To be useful, the data sets were then processed in matlab and filtered for anomalous events. These signals were also fitted with a sigmoid function to better quantify the risetime, and reject signals without this characteristic profile.

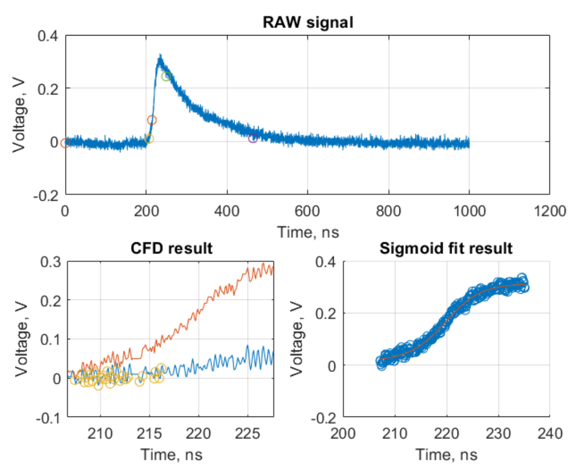

Figure 25: Sigmoid fit of waveform.

By collecting all of the appropriate events and calculating the risetime based on the sigmoid fit, the average risetime for each device was determined. These can be found in Table 1, along with the experiment voltages, and voltage threshold used in data processing.

Using the data collected from the triple GEMs, the beam could be spatially reconstructed, and the response of the detector with reference to the known location of the beam could

Device	C/A Volt. (V)	Dev. Volt. (V)	Thresh. (V)	Risetime (ns)
S13360-1325CS	520/540	56.5	0.003	39.364
S13370-3050CS	500/510	57.0	0.040	22.318
1x S14160-4050HS	500/510	44.0	0.040	39.682
4x S14160-4050HS	620/620	40.7	0.070	23.794
S14160-6050HS	500/500	43.0	0.020	42.304

Table 1: Preliminary device risetimes, after filtering events below the voltage threshold, and performing a sigmoid fit.

then be tested. This was done using a custom matlab script. A heatmap reconstruction of the beam on each SiPM from the best (most number of data points after processing) run of each device can be seen below.

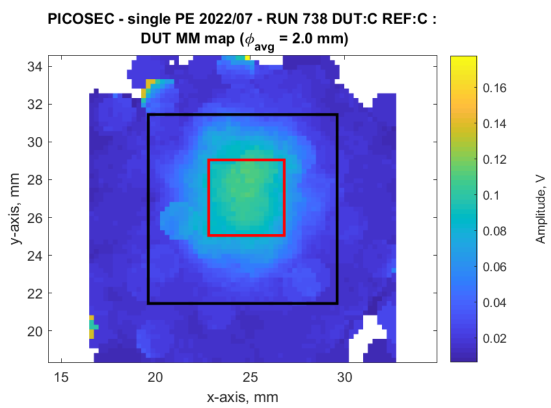

Figure 26: Spatially reconstructed signal location heatmap for (single) S14160-4050HS device.

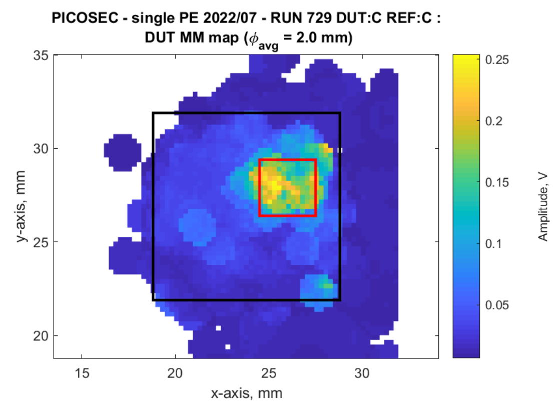

Figure 27: Spatially reconstructed signal location heatmap for S13370-3050CS device.

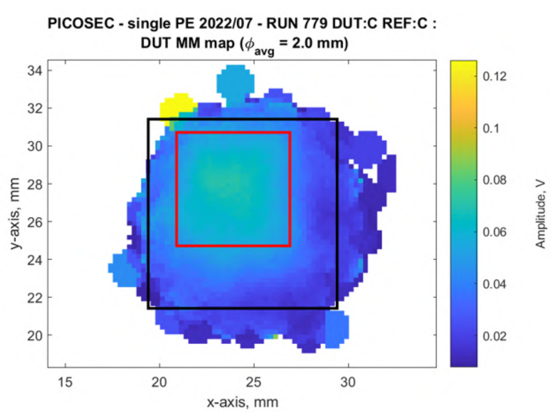

Figure 28: Spatially reconstructed signal location heatmap for S14160-6050HS device.

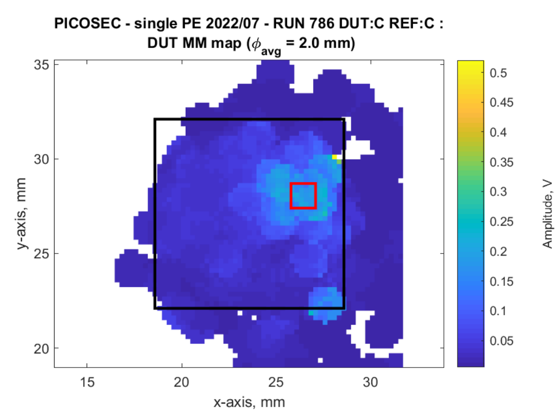

Figure 29: Spatially reconstructed signal location heatmap for S13360-1325CS device.

Device	C/A Volt. (V)	Dev. Volt. (V)	Threshold (V)	Res. (ns)
S13360-1325CS*	520/540	56.5	0.003	6.4244*
S13370-3050CS	500/510	57.0	0.040	9.5719
1x S14160-4050HS	500/510	44.0	0.040	7.3029
S14160-6050HS	500/500	43.0	0.020	9.8330

Table 2: Time resolution of each of the SiPM devices. Note that the resolution of S13360-1325CS is perhaps not accurate due to the extremely low number of events considered in this computation.

Note that the red box on each heatmap signifies the size of the SiPM device. These boxes were included in the figure by hand as an estimate as to where the SiPM is approximately located for reference. Note that the heatmaps in Figures 27 and 29 are quite patchy in comparison to the smooth colour gradient of the other two figures. This is due to the fact that the number of data points were comparatively small post the processing of the signal. In future testing, much longer runs should be taken in order to collect more usable data for these devices. Figures 26 and 28 have the expected shape of the heatmap. We expect the signal to be quite saturated inside the SiPM region. In such an experiment, we expect the Cherenkov cone to be about 6mm in diameter. Thus, we should expect to see a reduced signal up to 3mm away from the edge of the device, as an incident particle in this region will produce a Cherenkov radiation cone sufficiently wide to be faintly detected by the SiPM. This is best illustrated in Figure 26, where the majority of the signal can be seen to be roughly within 3mm of the red box representing the SiPM.

The time delay between the MCP triggering and SiPM signal was also measured. The spread in this time delay provides a measure of the timing resolution of the device. Note that each device had a significant number of counts that had almost zero time delay. It is believed that this zero time delay was due to either, in the most likely scenario, no signal being detected by the device in the time window after the MCP trigger (and hence being assigned a default value of 0), or there was some other spark/event occurring inside the device at the time of triggering. The code was manually adjusted to only consider events falling within a reasonable time delay based on the distance of the detector from the MCP to exclude as much noise as possible without overfitting. An example of this can be seen in Figure 30.

The time resolutions of each device under test can be found in Table 2.

Note that the preliminary risetimes computed earlier for the devices are quite slow. Using the spatial reconstruction data, the risetimes of the signals could also be improved. This was done by constraining the code to only consider signals that fell spatially inside the red box indicating the device. This would help to filter out noise (when an event is detected corresponding to a beam particle far from the location of the SiPM, it is likely that this is a noise event), and partially contained event (might have a worse risetime due to a weaker signal with longer duration). The downside of this mask is that it reduces the number of data points. Thus for our data sets, it was really only practical to apply this approach to run 738 for the S14160-4050HS device. In this case, the rise time went from being approximately 39.7ns in the preliminary analysis to approximately 24.3ns after this mask was applied.

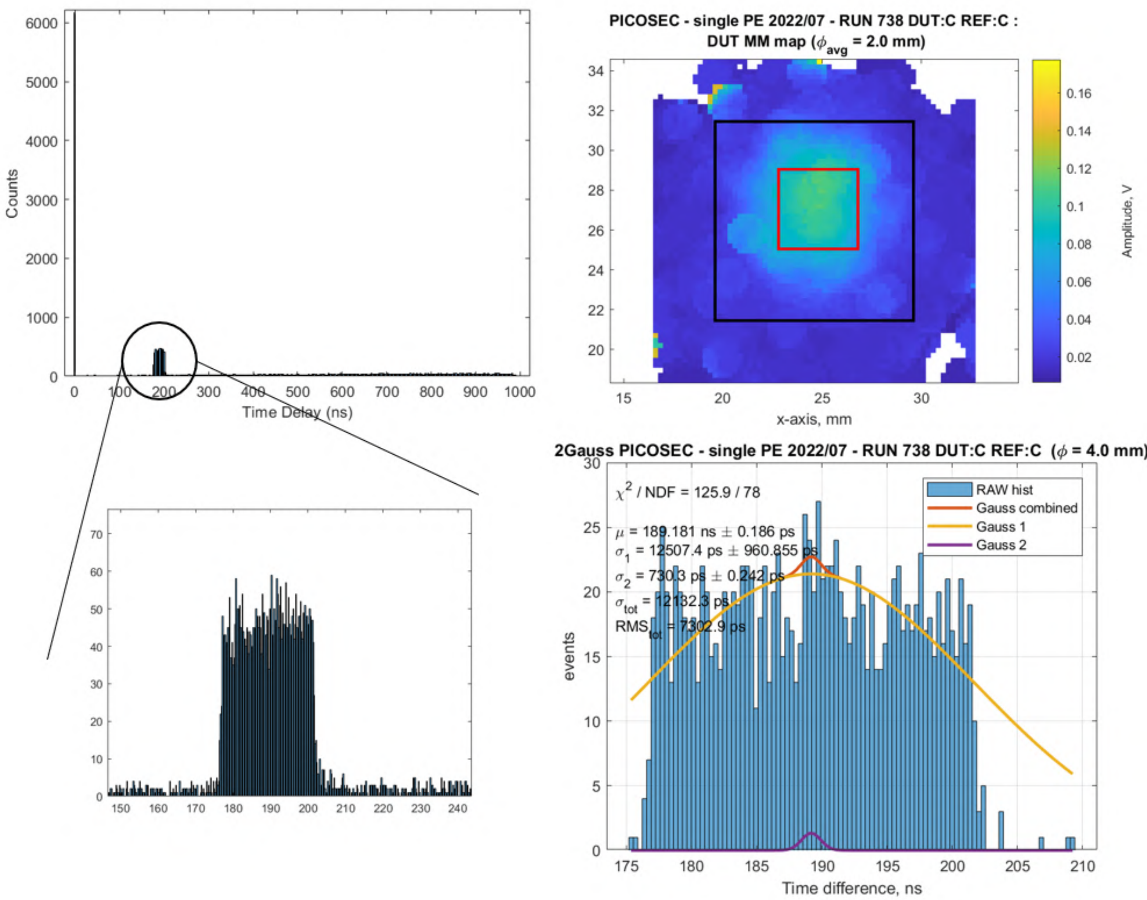

Figure 30: Time resolution computation for the S14160-4050HS device. Fitted curves here are irrelevant to this analysis.

To improve the risetime, other methods were also considered. One method was to use the integrated area of the signal and relate this to the risetime, allowing for further filtering of the signals. Another idea was to attempt to identify individual photon arrival events in the rising edge. As not all photons from a single arrive at our device at the same time, in theory, it would be possible to identify individual photons by observing small dips after a photon arrival in the rising edge of the signal due to the discharge of the device, before the next photon arrives. To do this, an attempt was made to use a numerical derivative of the rising edge of the signal to try and identify these individual photon events. However, this proved to yield little fruit due to the noise in the signal. Further avenues worth exploring would be performing some sort of fit or moving average of the signal to smooth out some of the noise, and then taking derivatives to see if there is still any useful information.

It is worth considering whether or not these risetimes are actually reasonable. According to the device specifications for the SiPMs, the rise time should be on the order of nanoseconds (see Figure 32). Thus, it appears that these risetimes are unexpectedly long.

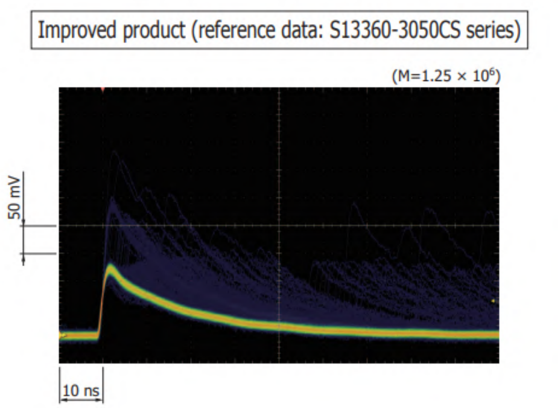

Figure 31: Pulse response of the S13370-3050CS device, manufacturer's specs. [2]

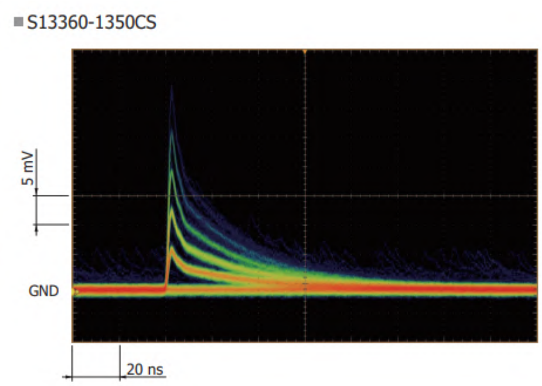

Figure 32: Typical response of the C12332-01 preamplifier, (demonstrated with the S13360-1350CS), manufacturer's specs. [3]

This quirk makes sense however, if one considers the physical process of photon production by the gas. This can be seen in Figure 33.

In this regard, the slow risetime in our signals makes sense, as the relaxation of the CF4 gas happens over a timescale comparable to the risetimes we measured in our devices. Thus, it would appear that the slow risetimes are a limitation of the physical process itself, rather than a device response issue.

4 Conclusion

In this experiment, we were able to measure the risetimes in the signals of five different SiPM devices. We have shown that these risetimes measure the relaxation time in the emission spectrum of the CF4 used to produce photons in the experiment, and not the response of the devices themselves. We were also able to use data from the triple GEM setup to spatially reconstruct a heatmap of the location of the muon events that were detected by

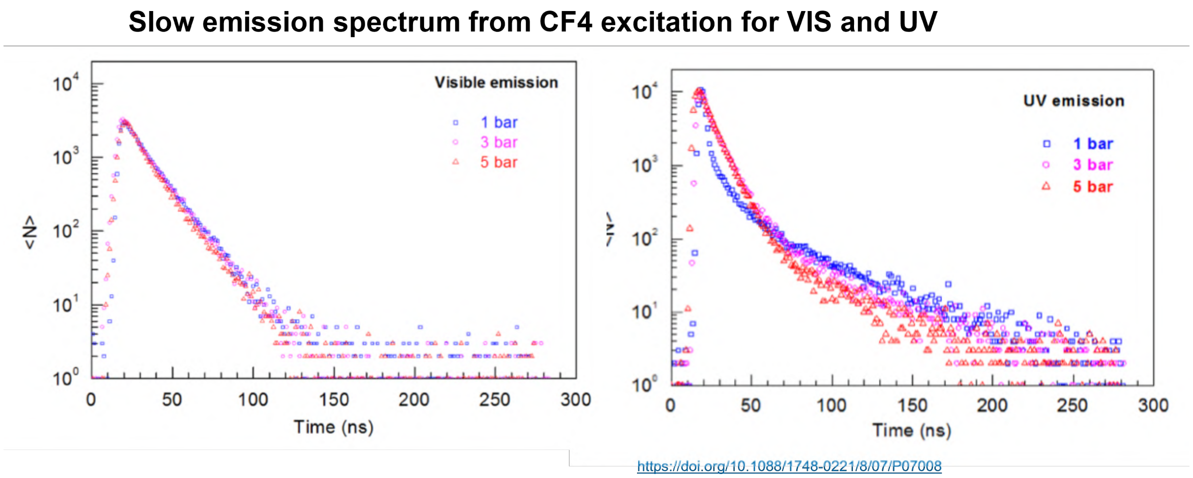

Figure 33: Emission relaxation time for CF4, for both visible and UV light. [4]

our device. We were then also able to compute the time resolution of each device. To have more confidence in the results, the experiment should be repeated with much longer runs (especially for the smaller devices that collect less light) to ensure the quantity of data is still sizeable after filtering and masking, allowing us to make clearer conclusions.

5 Acknowledgements

I would sincerely like to thank everyone in the GDD group for being exceptionally hospitable, generous, and patient during my stay at CERN. I learned an incredible amount about physics during my stay, and I feel like I have a much more holistic view of physics that I was perhaps lacking before, thanks to this experience. It was truly a once in a lifetime experience for me to take part in this program, and for that I will be forever thankful.

References

[1] Brunbauer, F. M. *SiPM readout of optical Picosec MM*, 2021, Presentation.

[2] Hamamatsu, *MPPC (multi-pixel photon counter) S13360 series Datasheet*, 2022, `https://www.hamamatsu.com/jp/en/product/optical-sensors/mppc/mppc_mppc-array/S13360-3050CS.html`.

[3] Hamamatsu, *Preamplifier C12332-01 Datasheet*, 2022, `https://www.hamamatsu.com/eu/en/product/type/C12332-01/index.html`.

[4] Margati L.M.S., Morozov A., Fraga M.M.F.R., Pereira L., Fraga F.A.F., *Effective decay time of CF4 secondary scintillation* JINST **8**, P07008 (2013).